Broadband sparse-array blind deconvolution using frequency-difference beamforming

Shima H. Abadi[a)]
Department of Mechanical Engineering, University of Michigan, Ann Arbor, Michigan 48109

H. C. Song
Marine Physical Laboratory, Scripps Institution of Oceanography, University of California,
San Diego, La Jolla, California 92093

David R. Dowling
Department of Mechanical Engineering, University of Michigan, Ann Arbor, Michigan 48109

Synthetic time reversal (STR) is a technique for blind deconvolution of receiving-array recordings of sound from an unknown source in an unknown multipath environment. It relies on generic features of multipath sound propagation. In prior studies, the pivotal ingredient for STR, an estimate of the source-signal's phase (as a function of frequency ω), was generated from conventional beamforming of the received-signal Fourier transforms, $P_j(\omega)$, $1 \leq j \leq N$, where N is the number of array elements. This paper describes how STR is implemented even when the receiving-array elements are many wavelengths apart and conventional beamforming is inadequate. Here, the source-signal's phase is estimated by beamforming $P_j^*(\omega_1)P_j(\omega_2)$ at the difference frequency $\omega_2 - \omega_1$. This extension of STR is tested with broadband signal pulses (11–19 kHz) and a vertical 16-element receiving array having a 3.75-m-spacing between elements using simple propagation simulations and measured results from the FAF06 experiment involving 2.2 km of down slope propagation from 46 to 92 m water depth. The cross-correlation coefficient between the source-broadcast and STR-reconstructed-signal waveforms for the simulations and experiments are 98% and 91%–92%, respectively. In addition, frequency-difference beamforming can be used to determine signal-path-arrival angles that conventional beamforming cannot. © *2012 Acoustical Society of America.*
[http://dx.doi.org/10.1121/1.4756920]

I. INTRODUCTION

When sound travels away from a source in the ocean, refraction within the water column and reflections from the ocean surface and bottom commonly lead to multipath propagation that causes signal distortion when a remote listening receiver records this sound. When the sound source is unknown, such signal distortion impedes source classification and identification by the listener. Blind deconvolution is the name given to the task of separately estimating the unknown waveforms for the original source signal and the source-to-receiver impulse response(s) from the recorded signal(s) when the acoustic environment is also unknown. This paper describes how synthetic time reversal (STR) and unconventional frequency-difference beamforming together provide an efficient means for blind deconvolution for signals recorded underwater when the receiver is a sparse array of hydrophones that is not suitable for conventional delay-and-sum plane-wave beamforming techniques and the received field cannot be modeled precisely as a superposition of plane waves propagating across the array aperture (i.e., modeling mismatch).

Blind deconvolution is frequently attempted in image processing and in situations involving multipath acoustic propagation; however, there are implementation differences. In ultrasonic image processing applications (see Taxt and Strand, 2001 or Yu *et al.*, 2012), the goal of blind deconvolution is to enhance image (signal) quality by correcting for an imperfect transfer function (commonly known as the point spread function). Here the number of receiving elements (i.e., the number of pixels) may greatly exceed the number of temporal samples—perhaps just a single image. In underwater acoustics, the goal of blind deconvolution is similar—improving signal quality—but the form of the input data is different; the number of receiving transducers N (a countable number) is typically much less than the number of temporal samples (thousands or even millions). The work reported here focuses on the later situation.

In general blind deconvolution is an ill-posed problem. In particular in underwater applications, blind deconvolution involves using N receiving-array recordings to estimate $N+1$ waveforms: N source-to-receiver transfer-function waveforms, and one source-signal waveform. Thus, a successful technique for blind deconvolution must incorporate additional information to reach unique and correct results. In past blind deconvolution efforts, this extra information has been developed from: Monte Carlo optimization and a well-chosen cost function (Smith and Finette, 1993), additional

---

[a)]Author to whom correspondence should be addressed. Electronic mail: shimah@umich.edu

measurements from a known source (Siderius *et al.*, 1997), higher order statistics (Broadhead and Pflug, 2000a,b), information criteria (Xinhua *et al.*, 2001), adaptive algorithms (Weber and Bohme, 2002; Sibul *et al.*, 2002), time frequency analysis (Martins *et al.*, 2002), multiple convolutions (Smith, 2003), an assumption about the probability density function of the signal (Roan *et al.*, 2003), and a least-squares criterion (Zeng *et al.*, 2009). The blind deconvolution technique used in this study, synthetic time reversal or STR (Abadi *et al.*, 2012), develops the requisite additional information from the assumption that sound is conveyed from the unknown source to the receiving array by modes or rays.

STR [also known as artificial time reversal (ATR) (Sabra and Dowling, 2004; Sabra *et al.*, 2010)] is a fully passive technique for blind deconvolution that does not involve iterative procedures, parameter searches, or optimizations. It is potentially fast and efficient enough for real-time applications. Its computational cost only marginally exceeds that of computing forward and inverse fast-Fourier transforms (FFTs) of the recorded signals. STR is successful when the acoustic propagation is well-described by a modal sum in a low-frequency region (375–625 Hz) and the receiving array is vertical and spans the water column (Sabra and Dowling, 2004), and when the acoustic propagation is well described by a ray-path sum in a mid-frequency region (1–4 kHz) and the receiving array is vertical with sufficient element density so that conventional delay-and-sum beamforming can be used to distinguish ray-path-arrival directions (Sabra *et al.*, 2010; Abadi *et al.*, 2012).

The purpose of this paper is two-fold: first, present STR blind deconvolution results for source signal estimation when the receiving array is sparse and conventional beamforming is not appropriate for the frequency band of interest (11–19 kHz), and second, introduce an unconventional beamforming technique based on manufacturing frequency differences from the array recordings that allows STR to be successful with sparse array measurements in the presence of modeling mismatch. STR signal reconstruction results are reported for simple simulations involving three acoustic paths, and then for propagation measurements made during the FAF06 (Focused Acoustic Field 2006) experiment conducted in the Mediterranean Sea (Song *et al.*, 2009; Song *et al.*, 2010). In both cases the signal is a tapered linear frequency modulation (LFM) chirp (11–19 kHz), and the receiving array is vertical with 16 elements spaced almost 40 signal-center-frequency wavelengths apart. Interestingly, the unconventional frequency-difference beamforming technique is successful finding ray-path directions when conventional beamforming is not, and likely has applications beyond STR blind deconvolution.

The remainder of this paper is divided into four sections. Section II presents the mathematical formulation of ray-based STR when combined with frequency-difference beamforming. Section III presents STR results from simulated acoustic propagation in a simple environment with three ray paths that mimics the FAF06 experiment. Section IV presents STR results for FAF06 probe-signal broadcasts that

were recorded at a source-array range of 2.2 km. Section V summarizes this research effort, and states the conclusions drawn from it.

II. SYNTHETIC TIME REVERSAL WITH FREQUENCY-DIFFERENCE BEAMFORMING

STR is a simple array-signal-processing technique for simultaneously estimating the waveforms of the unknown source signal and the unknown source-to-array transfer functions in an unknown multipath environment. As described below, the critical step in STR is isolating the phase of the unknown source signal from the measured signals. The development of STR with conventional beamforming for isolating the signal phase via a mode-shape weighting or ray-path weighting of the array measurements is described elsewhere (Sabra and Dowling, 2004; Sabra *et al.* 2010; Abadi *et al.*, 2012). The following development follows that in Sabra and Dowling (2004) but emphasizes and motivates STR's use with frequency-difference beamforming.

A. Basic elements of synthetic time reversal

The inputs for STR are the measured waveforms $p_j(t)$ from the N receiving-array elements located at $\vec{r}_j$ ($1 \leq j \leq N$), and an assumption about of the character of the acoustic propagation; it is either a sum of modes or rays. In the present study, the ray assumption is made, as is appropriate for high-frequency underwater-sound signals (11–19 kHz). The Fourier transforms, $P_j(\omega)$, of the received signals can be written in terms of the Fourier transform of the signal, $S(\omega) = |S(\omega)|e^{i\varphi_s(\omega)}$, and the environment's Green's function, $G(\vec{r}_j, \vec{r}_s, \omega)$ (the Fourier transform of the environment's impulse response),

$$\frac{1}{2\pi}\int_{-\infty}^{+\infty} p_j(t)e^{i\omega t}dt = P_j(\omega) = G(\vec{r}_j, \vec{r}_s, \omega)|S(\omega)|e^{i\varphi_s(\omega)},$$

(1)

when the acoustic propagation is independent of time for the duration of the signal. Here, $\vec{r}_s$ is the unknown source location and $\varphi_s(\omega)$ is the source signal's phase as a function of frequency ω.

The formulation of STR begins by developing an estimate $G(\vec{r}_j, \vec{r}_s, \omega)$ from $P_j(\omega)$ alone. The first step is a simple normalization of $P_j(\omega)$ in Eq. (1) that eliminates the signal amplitude,

$$\tilde{P}_j(\omega) = \frac{P_j(\omega)}{\sqrt{\sum_{j=1}^{N}|P_j(\omega)|^2}}$$

$$= \frac{G(\vec{r}_j, \vec{r}_s, \omega)}{\sqrt{\sum_{j=1}^{N}|G(\vec{r}_j, \vec{r}_s, \omega)|^2}}e^{i\varphi_s(\omega)}.$$

(2)

To produce a normalized estimate of $G(\vec{r}_j, \vec{r}_s, \omega)$ from Eq. (2), the signal's phase $\varphi_s(\omega)$ must be estimated and

removed from the right side of Eq. (2). This is the pivotal step in STR. However, in the present investigation, the vertical aperture and/or element density of the receiving array are assumed insufficient to resolve individual propagating modes or rays in the sound channel. In particular, the receiving array is extremely sparse (many wavelengths between array elements) so that a multitude of side lobes (i.e., spatial aliasing) degrade the utility of conventional plane-wave beamforming and the plane-wave-signal assumption may not hold across the entire aperture over the frequency band of interest. Thus, prior implementations of STR will not be successful. This parametric situation occurs in studies of underwater acoustic communication when signals with frequencies around 10 kHz are recorded with array elements that are well-separated (e.g., a few meters) to provide spatial diversity, as presented in Rouseff *et al.* (2001), Siderius *et al.* (2007), or Song *et al.* (2009) and Song *et al.* (2010). Moreover, in applications of blind deconvolution, the received signal from the unknown source may be ill suited for the receiving array's configuration; therefore, extension of STR to sparse arrays enhances its potential utility.

Thus, an unconventional beamforming technique for isolating $\varphi_s(\omega)$ is developed that manufactures lower-frequency signal information from the higher-frequency broadband signal recordings $P_j(\omega)$. This unconventional technique involves delay-and-sum beamforming of the measured-field product $P_j^*(\omega_1)P_j(\omega_2)$ at the difference frequency $\omega_2 - \omega_1$, so it is referred to herein as frequency-difference beamforming. It may be valuable for array-signal-processing applications beyond STR.

B. Frequency-difference beamforming

Frequency-difference beamforming stems from the following ray-path approximation for the sound channel's impulse response:

$$G(\vec{r}_j, \vec{r}_s, \omega) = \sum_{l=1}^{L} A_{lj} \exp\{i\omega r_{lj}/\bar{c}\}. \tag{3}$$

Here L is the number of ray paths between the sound source and receiving array, $1 \leq l \leq L$, A_{lj} is an amplitude for each ray to each receiver, r_{lj} is the effective length of each ray path to each receiver, and $\bar{c}$ is an appropriate average sound speed. In general, A_{lj} is a complex number and may depend on frequency but such dependence is neglected here. An equivalent formulation based on a modal sum, instead of Eq. (3), is likely possible but is not discussed here. Combining Eqs. (2) and (3) produces

$$\tilde{P}_j(\omega) = \frac{e^{i\varphi_s(\omega)}}{\sqrt{\sum_{j=1}^{N} |G(\vec{r}_j, \vec{r}_s, \omega)|^2}} \sum_{l=1}^{L} A_{lj} \exp\left\{i\frac{\omega r_{lj}}{\bar{c}}\right\}. \tag{4}$$

This equation explicitly shows how the frequency ω influences phase, even though the path amplitudes A_{lj}, path lengths r_{lj}, and average sound speed $\bar{c}$ are unknown. Equation (4) can be developed into an expression that includes a frequency difference that is small enough for plane-wave beamforming: evaluate Eq. (4) at two different frequencies $\omega_2 > \omega_1$, complex conjugate the ω_1-evaluation, and form the normalized field product

$$\tilde{P}_j^*(\omega_1)\tilde{P}_j(\omega_2) = \frac{\exp\{i(\varphi_s(\omega_2) - \varphi_s(\omega_1))\}}{\sqrt{\sum_{j=1}^{N} |G(\vec{r}_j, \vec{r}_s, \omega_1)|^2} \sqrt{\sum_{j=1}^{N} |G(\vec{r}_j, \vec{r}_s, \omega_2)|^2}} \sum_{l=1}^{L} \sum_{m=1}^{L} A_{lj}^* A_{mj} \exp\left\{i\frac{\omega_2 r_{mj} - \omega_1 r_{lj}}{\bar{c}}\right\}. \tag{5}$$

The phase relationship embodied in Eq. (5) is of interest because the source phase difference, $\varphi_s(\omega_2) - \varphi_s(\omega_1)$, appears on the right side, and because the exponential phase inside the double sum is proportional to $\omega_2 - \omega_1$ when $m = l$. In Eq. (5) the square-root factors are real functions, so equating phases in Eq. (5) leads to

$$\arg\left(\tilde{P}_j^*(\omega_1)\tilde{P}_j(\omega_2)\right) = \varphi_s(\omega_2) - \varphi_s(\omega_1)$$
$$+ \arg\left[\sum_{l=1}^{L} A_{lj}^* A_{lj} \exp\left\{i\frac{(\omega_2 - \omega_1) r_{lj}}{\bar{c}}\right\}\right]$$
$$+ \sum_{l \neq m}^{L,L} A_{lj}^* A_{mj} \exp\left\{i\frac{(\omega_2 r_{mj} - \omega_1 r_{lj})}{\bar{c}}\right\}\right]. \tag{6}$$

Here, the double sum over ray paths has been separated into diagonal ($l = m$) and off-diagonal ($l \neq m$) terms. The diagonal terms in Eq. (6) explicitly include the frequency difference $\omega_2 - \omega_1$ and take the following form:

$$\text{diagonal terms} = \sum_{l=1}^{L} B_{lj} \exp\left\{i\frac{(\omega_2 - \omega_1) r_{lj}}{\bar{c}}\right\}, \tag{7}$$

where $B_{lj} = A_{lj}^* A_{lj}$ (no sum implied). Interestingly, Eq. (7) is functionally the same as Eq. (3) with ω replaced by $\omega_2 - \omega_1$. In both Eqs. (3) and (7) the r_{lj} correspond to L signal-paths having arrival angles θ_l at the receiving array. Thus, conventional delay-and-sum beamforming of the field product $\tilde{P}_j^*(\omega_1)\tilde{P}_j(\omega_2)$ at the difference frequency $\omega_2 - \omega_1$ may yield a useful estimate of the signal phase difference $\varphi_s(\omega_2) - \varphi_s(\omega_1)$ when the beam steering angle is equal to θ_l, and

the off-diagonal terms in Eq. (6) are unimportant as will be described below.

In the current investigation, such a signal-phase-difference estimate is developed from

$$b(\theta,\omega_1,\omega_2) = \sum_{j=1}^{N} \tilde{P}_j^*(\omega_1)\tilde{P}_j(\omega_2)$$
$$\times \exp\{-i(\omega_2 - \omega_1)\tau(\theta,\vec{r}_j)\}, \quad (8)$$

where b is the frequency-difference beamforming output, τ is the time delay, and θ is the beam steering angle defined with respect to broadside ($\theta = 0$). If $\tilde{P}_j^*(\omega_1 = 0)$ is a non-zero constant that is independent of j, then Eq. (8) reduces to conventional delay-and-sum beamforming in the limit $\omega_1 \to 0$,

$$\lim_{\omega_1 \to 0} b(\theta,\omega_1,\omega_2) = b(\theta,0,\omega_2)$$
$$\propto \sum_{j=1}^{N} \tilde{P}_j(\omega_2)\exp\{-i\omega_2\tau(\theta,\vec{r}_j)\}. \quad (9)$$

For evenly spaced elements along a linear vertical array (the array geometry of interest here), the time delays in an isospeed sound channel are simply related to the beam steering angle,

$$\tau(\theta,\vec{r}_j) = \tau(\theta,z_j) \cong (j-1)(d/\bar{c})\sin\theta, \quad (10)$$

where d is the distance between array elements. When there is significant vertical variation in the channel's sound speed

$c(z)$, the time delays $\tau(\theta,z_j)$ can be selected in accordance with ray group velocities to account for the curvature of the incoming wavefronts (see Dzieciuch *et al.*, 2001; Roux *et al.*, 2008). However, In blind deconvolution, $c(z)$ is considered unknown. So, an appropriate constant value of $\bar{c}$ will be used to generate the results in the Secs. III and IV.

C. Structure of the field product

The mathematical structure of the field product in Eq. (8) can be illustrated by using Eqs. (1) and (3) in the simple case of two ray paths ($L = 2$) when the A_{lj} are real coefficients. First combine Eqs. (1) and (3) with $L = 2$, to find

$$P_j(\omega) = S(\omega)(A_{1j}\exp\{i\omega r_{1j}/\bar{c}\} + A_{2j}\exp\{i\omega r_{2j}/\bar{c}\}). \quad (11)$$

Thus, the field product becomes

$$P_j^*(\omega_1)P_j(\omega_2) = S^*(\omega_1)S(\omega_2)\left(A_{1j}\exp\left\{\frac{i\omega_1 r_{1j}}{\bar{c}}\right\}\right.$$
$$+ A_{2j}\exp\left\{\frac{i\omega_1 r_{2j}}{\bar{c}}\right\}\right)^*\left(A_{1j}\exp\left\{\frac{i\omega_2 r_{1j}}{\bar{c}}\right\}\right.$$
$$\left. + A_{2j}\exp\left\{\frac{i\omega_2 r_{2j}}{\bar{c}}\right\}\right), \quad (12)$$

which, after some algebra, reduces to

$$P_j^*(\omega_1)P_j(\omega_2) = S^*(\omega_1)S(\omega_2)\left(A_{1j}^2\exp\left\{i\frac{\Delta\omega}{\bar{c}}r_{1j}\right\} + A_{2j}^2\exp\left\{i\frac{\Delta\omega}{\bar{c}}r_{2j}\right\}\right.$$
$$\left. + 2A_{1j}A_{2j}\cos\left[\left(\frac{\omega_1 + \frac{1}{2}\Delta\omega}{\bar{c}}\right)(r_{2j} - r_{ij})\right]\exp\left\{i\frac{\Delta\omega}{\bar{c}}\left(\frac{r_{1j} + r_{2j}}{2}\right)\right\}\right), \quad (13)$$

where $\Delta\omega = \omega_2 - \omega_1$. The first two terms inside the big parentheses on the right side of Eq. (13) are the diagonal terms of the field product. They follow the form of Eq. (7) and their phases only depend on $\Delta\omega$, $\bar{c}$, and the two ray path lengths. When $P_j^*(\omega_1)P_j(\omega_2)$ from Eq. (13) is beamformed at the difference frequency, $\Delta\omega$, these diagonal terms will make a contribution to $b(\theta,\omega_1,\omega_2)$ that does not depend on ω_1.

On the other hand, the third term inside the big parentheses on the right side of Eq. (13) results from combining the two off-diagonal terms of the field product. It depends on $\Delta\omega$, ω_1, $\bar{c}$, and the sum and difference of the two ray path lengths. Thus, when $P_j^*(\omega_1)P_j(\omega_2)$ from Eq. (13) is beamformed at the difference frequency, $\Delta\omega$, this term will change as ω_1 is varied. Such ω_1-dependent contributions to $b(\theta,\omega_1,\omega_2)$ can be considered structured interference or noise as will be evident in the simulation results in Sec. III.

In general, when L ray paths connect the source and the receiving array, the number of desired ω_1-independent diagonal terms (signal) increases like L while the number of undesired ω_1-dependent off-diagonal-term contributions (noise) increases like $L(L-1)/2$. Thus, for an arbitrary L, there may be an inherent limit to frequency-difference beamforming's utility since its signal-to-noise ratio may decrease like $(L-1)^{-1}$ with increasing L. However, this limit—if it exists—has not been reached by either the simulation or experimental results presented in Secs. III and IV.

D. Implementation of STR with frequency-difference beamforming

With this understanding of frequency-difference beamforming, the phase relationship embodied in Eq. (8) is

$$\arg\left(b(\theta,\omega_1,\omega_2)\right) = \varphi_s(\omega_2) - \varphi_s(\omega_1) + \arg\left(\sum_{j=1}^{N}\sum_{l=1}^{L}\sum_{m=1}^{L} A_{lj}^* A_{mj}\exp\left\{i\left(\frac{(\omega_2 r_{mj} - \omega_1 r_{lj})}{\bar{c}} - (\omega_2 - \omega_1)\tau(\theta,\vec{r}_j)\right)\right\}\right), \quad (14)$$

where the final term involving the triple sum can be assumed approximately a constant angle, K, independent of ω_1 and ω_2 when θ coincides with θ_l, a signal-path arrival angle, and the off-diagonal terms of the field product are unimportant. Under these conditions, an estimate of the source-signal phase can then be developed throughout the signal bandwidth by recursively applying Eq. (14) after assuming an initial signal phase of zero. For example, if $P_j(\omega)$ is obtained from an FFT of $p_j(t)$ at evenly spaced frequencies ω_q, $1 \le q \le Q$, then the source-signal phase estimate $\hat{\varphi}(\omega_q)$ produced by Eq. (14) at these frequencies when $\theta = \theta_l$ is

$$
\begin{aligned}
\hat{\varphi}_s(\omega_1) &= 0, \\
\hat{\varphi}_s(\omega_2) &= \arg\Big(b(\theta_l, \omega_1, \omega_2)\Big) - K, \\
\hat{\varphi}_s(\omega_3) &= \arg\Big(b(\theta_l, \omega_2, \omega_3)\Big) + \varphi_s(\omega_2) - K = \arg\Big(b(\theta_l, \omega_2, \omega_3)\Big) + \arg\Big(b(\theta_l, \omega_1, \omega_2)\Big) - 2K, \\
&\vdots \\
\hat{\varphi}_s(\omega_q) &= \arg\Big(b(\theta_l, \omega_{q-1}, \omega_q)\Big) + \varphi_s(\omega_{q-1}) + K = \sum_{p=2}^{q} \arg\Big(b(\theta_l, \omega_{p-1}, \omega_p)\Big) - (q-1)K, \\
&\vdots \\
\hat{\varphi}_s(\omega_Q) &= \arg\Big(b(\theta_l, \omega_{Q-1}, \omega_Q)\Big) + \varphi_s(\omega_{Q-1}) = \sum_{p=2}^{Q} \arg\Big(b(\theta_l, \omega_{p-1}, \omega_p)\Big) - (Q-1)K.
\end{aligned}
\tag{15}
$$

Although the terms on the right involving K remain unknown, they lead to a phase contribution to $\hat{\varphi}_s(\omega)$ that is proportional to frequency, and such a phase contribution merely offsets the time origin of the STR-reconstructed waveforms. Therefore, STR cannot be used to determine absolute timing information, but the STR-determined waveform shapes are independent of K when it is constant.

The source-signal phase estimate $\hat{\varphi}_s(\omega)$ can be combined with (2) to produce a normalized estimate of the environment's Green's function

$$
\begin{aligned}
\hat{\tilde{G}}(\vec{r}_j, \vec{r}_s, \omega) &= \tilde{P}_j(\omega) \exp\{-i\hat{\varphi}_s(\omega)\} \\
&= \tilde{G}(\vec{r}_j, \vec{r}_s, \omega) \exp\{i\varphi_s(\omega) - i\hat{\varphi}_s(\omega)\}.
\end{aligned}
\tag{16}
$$

From here, an estimate of the Fourier transform of the source signal, $\hat{S}(\omega)$, can be obtained by using $\hat{\tilde{G}}(\vec{r}_j, \vec{r}_s, \omega)$ from Eq. (16), for back-propagation,

$$
\hat{S}(\omega) = \sum_{j=1}^{N} \hat{\tilde{G}}^*(\vec{r}_j, \vec{r}_s, \omega) P_j(\omega),
\tag{17}
$$

or inverse filtering,

$$
\hat{S}(\omega) = \frac{1}{N} \sum_{j=1}^{N} P_j(\omega) / \hat{\tilde{G}}(\vec{r}_j, \vec{r}_s, \omega);
\tag{18}
$$

they are identical for STR (see Sabra and Dowling 2004). Finally, an inverse Fourier transform of Eq. (16), and Eq. (17) or (18) recovers the source-to-array impulse responses and estimated source-signal waveform in the time domain, for example:

$$
\hat{s}(t) = \int_{-\infty}^{+\infty} \hat{S}(\omega) e^{-i\omega t} d\omega.
\tag{19}
$$

This formulation of STR benefits in three important ways from the inclusion of frequency-difference beamforming. First, the frequency difference used in Eq. (8) is only limited by the bandwidth of the signal and the spacing between FFT frequency samples; thus, it may often be chosen to suit the situation at hand. For example, in terms of cyclic frequency, f, these limits are $12.2 \, \text{Hz} \le f_2 - f_1 \le 8 \, \text{kHz}$ for the STR performance results shown in the next two sections. In fact, the frequency difference can be varied to resolve multiple signal arrival directions having nearly the same arrival angle, even when these paths are not identifiable with conventional beamforming (see Figs. 4 and 11). And second, when several signal propagation paths reach the receiving array at nearly the same angle, θ, a small value of the frequency difference may be chosen so that the receiving array does not distinguish these paths. In this case, when the beam steering angle is θ, the frequency-difference beamforming estimate, $\hat{\varphi}_s(\omega)$, of the source-signal phase from Eq. (12) is based on the average of these propagation paths, and STR blind deconvolution results may be excellent even though no single propagation path is resolved (see Figs. 6 and 10). Finally, the lower frequency ($\omega_2 - \omega_1$) produced from frequency-difference beamforming makes the STR process and beamforming more robust to potential mismatch between the actual measured field and the plane-wave assumption made across a sparse large-aperture array (see Figs. 1 and 2).

III. STR RESULTS FROM SIMPLE BROADBAND PROPAGATION SIMULATIONS

To determine the possible performance of STR in conjunction with frequency-difference beamforming, broadband simulations are undertaken that approximately mimic the signals and geometry of the FAF06 experiment. The acoustic environment is a 92-m-deep range-independent ideal waveguide with a uniform sound speed of 1500 m/s having a flat
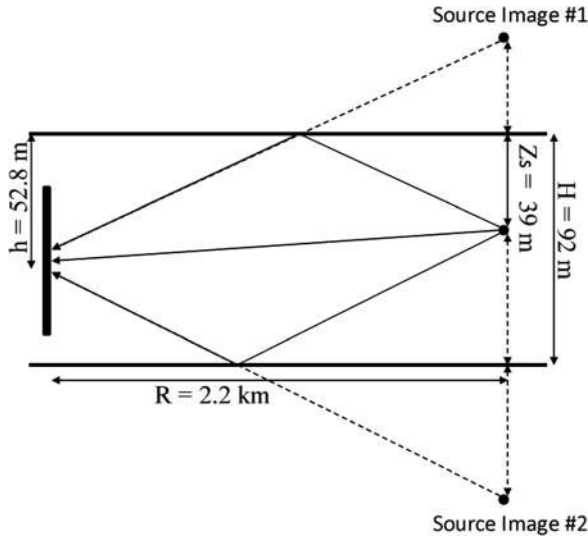
FIG. 1. Ideal sound channel that supports three propagation paths using the method of images. The source signal is a cosine tapered linear frequency modulation (LFM) sweep from 11 to 19 kHz and is broadcast from a depth of $z_s = 39$ m. The receiving array is 2.2 km away from the source and centered at a depth of 52.8 m. It consists of 16 hydrophones spanning a 56.25 m aperture with element spacing of 3.75 m (almost 40 wavelengths at the signal's center frequency of 15 kHz).

surface and bottom (see Fig. 1). The source at 39 m depth broadcasts a 60 ms cosine-tapered LFM chirp from 11 to 19 kHz. The linear vertical receiving array is located 2.2 km away from the source and centered at a depth of 52.8 m. It is composed of 16 elements spaced $d = 3.75$ m apart for an overall array length of $L_A = (N-1)d = 56.25$ m. At the source-signal center frequency (15 kHz), the element spacing corresponds to 37.5 wavelengths, making the array extremely sparse. Only the three ray paths shown in Fig. 1 are considered in these simulations using the method of images to ensure that the channel's delay spread is much smaller than the signal duration, as in the case of the FAF06 experiment. The results of the simulations are provided in Figs. 2–6. Note that the field received by the sparse array cannot be modeled precisely as three propagating plane waves for the current geometry and high frequency signal because the source is in the near field of the array at the signal's center frequency wavelength of $\lambda = 10$ cm. Following Kinsler *et al.* (2000) or equivalently Ziomek (1993), the array's far-field is reached (in free space) when $L_A^2/4\lambda r$ is comfortably less than unity, but for the geometry considered here with $r = 2.2$ km this parameter is greater than 1, $L_A^2/4\lambda r = (56.25\,\text{m})^2/[4(0.1\,\text{m})2200\,\text{m}] \approx 3.6$.

Figures 2, 3, 4, and 5 illustrate the performance of conventional and frequency-difference beamforming with $\bar{c} = 1500$ m/s. First, Fig. 2 shows the results of conventional plane-wave delay-and-sum beamforming of the array-recorded signals as a function of frequency, $f = \omega/2\pi$ (in Hz), over the bandwidth of the signal (11–19 kHz) and the beam steering angle (from $-90°$ to $90°$). As expected for a sparse receiving array along with mismatch in modeling (i.e., the existence of wave front curvature), the results are featureless. By comparison, the frequency-difference beamforming results, developed from Eq. (8) and shown in Fig. 3, display a clearer structure. The five panels in Fig. 3 show the same range of frequency (horizontal axis), $f_1 = \omega_1/2\pi$, each representing five increasing frequency differences, $\Delta f = (\omega_2 - \omega_1)/2\pi$: (a) 12.21 Hz, (b) 48.83 Hz, (c) 195.3 Hz, (d) 781.25 Hz, and (e) 1562.5 Hz. Since the sampling rate is 50 kHz and the FFT size is chosen as 4096 points, the result for the lowest possible frequency difference, $\Delta f = 12.21$ Hz, is shown in Fig. 3(a). The angular width of the broad central ridge in this panel is consistent with a linear array having $kL_A = 2.87$, where k is the wave number based on the frequency difference, $k = 2\pi\Delta f / \bar{c} = 0.0511$ m^{-1}, and L_A is 56.25 m. Figure 3(b) shows a similar result with $\Delta f = 48.83$ Hz, a factor of 4 increase in the frequency difference over that in Fig. 3(a). Here, the central ridge has narrowed in accordance with an increase in frequency. And, as anticipated from the discussion of Eq. (13), some intermittent side lobes from the off-diagonal terms of the field product emerge. Figure 3(c) shows a result with $\Delta f = 195.3$ Hz, a factor of 4 increase in the frequency difference above that in Fig. 3(b). Here again, the central ridge in the frequency-difference beamforming result shows a corresponding increase in resolution. However, this resolution is not yet sufficient to identify the angles of the three simulation ray paths. Perhaps more interesting in Fig. 3(c) is the increased prominence of the side lobes from the off-diagonal terms of the field product, which now appear as curving structures that enhance or distort the central ridge in Fig. 3(c). At this frequency difference (195.3 Hz), the array-element spacing is approximately $\lambda/2$, so the remaining panels of Fig. 3 display an increasingly narrower angular range to prevent repetition of the side lobe pattern (i.e., spatial aliasing). Figure 3(d) shows results with $\Delta f = 781.25$ Hz, a factor of 4 increase in the frequency difference above that shown in Fig. 3(c). At this frequency difference, the side lobes from the off-diagonal terms of the field product are stronger, and the horizontal central ridge is more uneven. Figure 3(e) shows a result with $\Delta f = 1562.50$ Hz, a factor of 2 increase in the frequency difference above that of
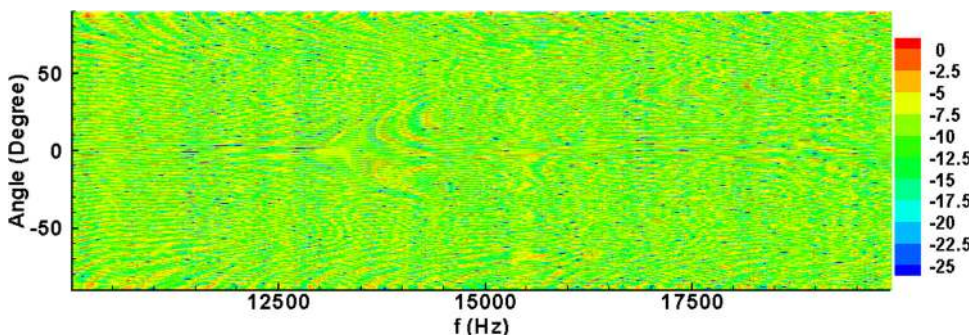

FIG. 2. (Color online) Conventional plane-wave beamforming output $B(\theta,f) = |b(\theta,0,2\pi f)|^2$ from Eq. (9) for the simulated signals as a function of look angle θ and frequency f in the signal bandwidth (11–19 kHz) in dB scale.
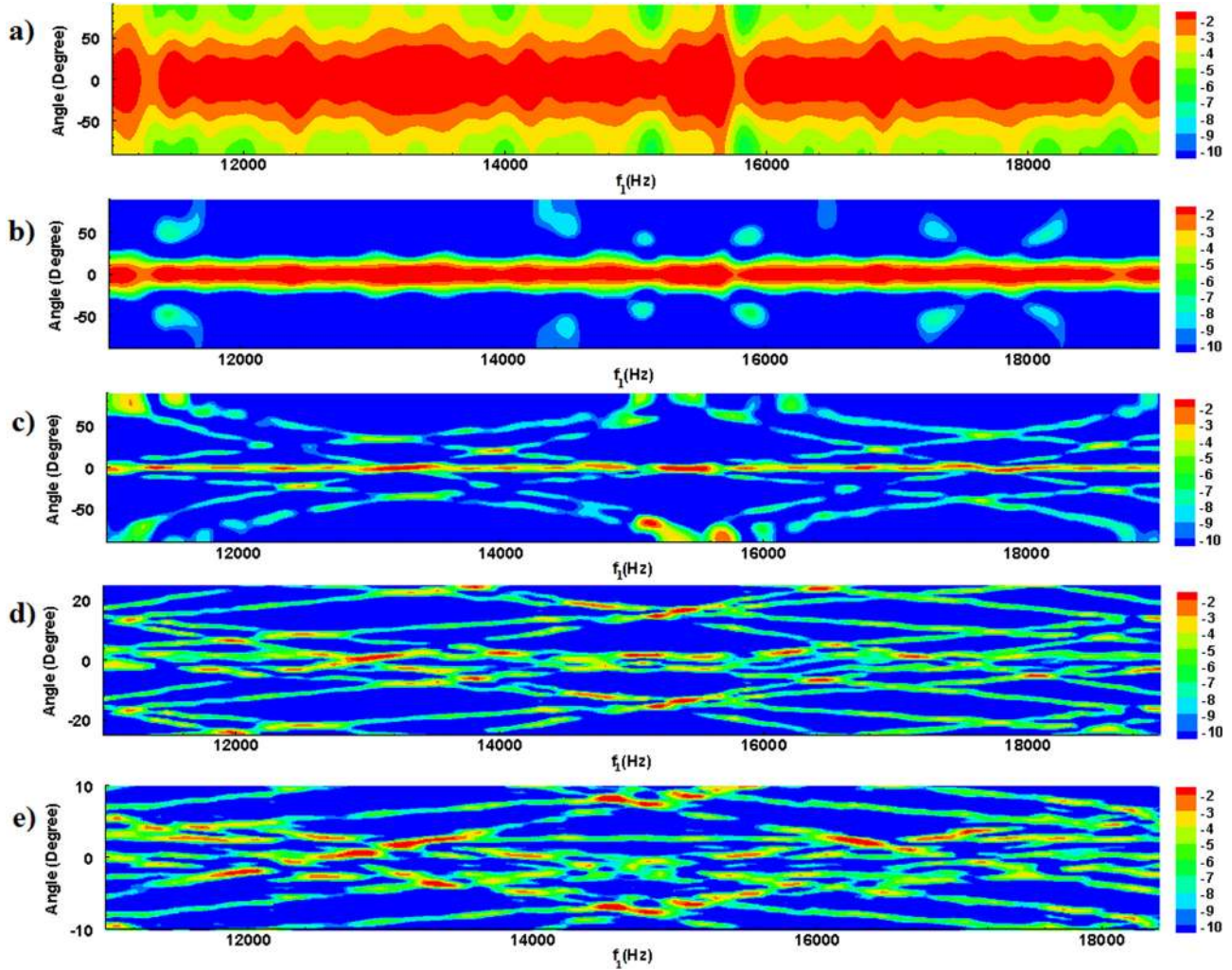
FIG. 3. (Color online) Unconventional frequency-difference beamforming output $B(\theta, f_1, \Delta f) = |b(\theta, 2\pi f_1, 2\pi f_2)|^2$ from Eq. (8) for the simulated signals as a function of look angle θ and frequency $f_1 = \omega_1/2\pi$ from 11 to 19 kHz with various frequency-differences: (a) $\Delta f = 12.21$ Hz, (b) $\Delta f = 48.83$ Hz, (c) $\Delta f = 195.31$ Hz, (d) $\Delta f = 781.25$ Hz, and (e) $\Delta f = 1562.5$ Hz. Note that the angular range of panels (d) and (e) is reduced to capture the output structure of frequency-difference beamforming near $\theta = 0°$ for the high frequency-difference cases.
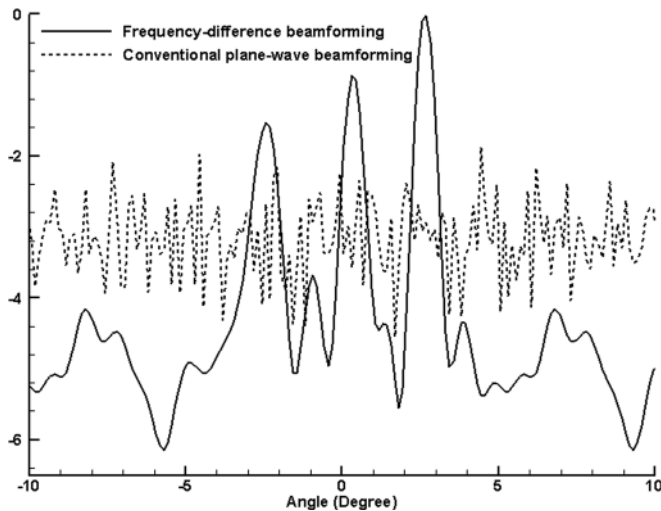

FIG. 4. Beamforming results incoherently summed over the frequency band using the simulated signals: $\sum_f B(\theta, f)$ or $\sum_{f_1} B(\theta, f_1, \Delta f)$. Frequency-difference beamforming with $\Delta f = 1562.5$ Hz (solid line) from Fig. 3(e) clearly indicates signal-arrival directions whereas conventional plane-wave beamforming (dash line) from Fig. 2 does not. The three peaks correspond to the three ray-path arrival angles (−2.4°, 0.3°, and 2.6°) of the propagation simulations, respectively.

Fig. 3(d). At this frequency difference, kL_A (as defined above) is almost 370 and the receiving array's angular resolution is about a degree near broadside. Although it is difficult to identify in the mix of slanted side lobes in Fig. 3(e), there are three horizontal bands of varying magnitude due to the diagonal terms of the field product that lie within $\pm 3°$ and correspond to the three simulation ray paths (see Fig. 4).

The angles of the three simulation ray paths may be recovered from the frequency-difference beamforming result shown in Fig. 3(e) when the individual frequency output is integrated over the bandwidth of the signal. Within such an integration, the persistent contribution of the field product's diagonal terms reinforces their prominence while the slanting side lobes seen in Fig. 3 from the field product's off-diagonal terms disperses their impact. The results of such an integration are shown in Fig. 4 where the dashed curve is for conventional beamforming while the solid curve is for frequency-difference beamforming at $\Delta f = 1562.50$ Hz. The conventional beamforming result obtained by integrating horizontally through Fig. 2 fails to show any prominent ray path direction. On the other hand, the integrated frequency-difference beamforming result clearly displays three peaks at
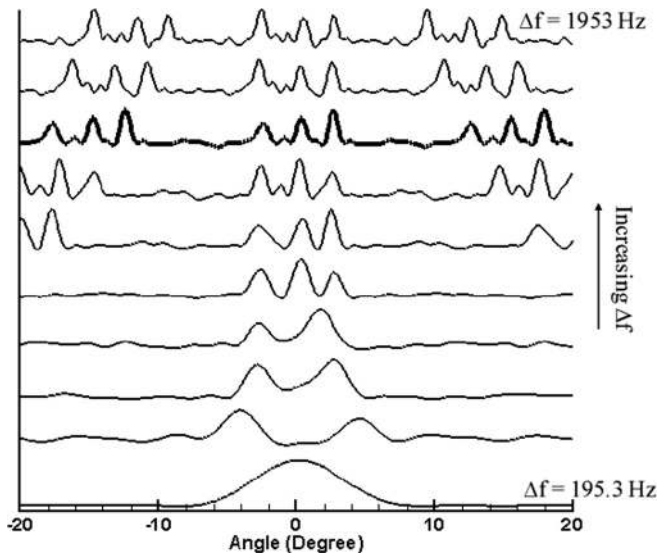
Abadi *et al.*: Blind deconvolution and sparse-array beamforming

FIG. 5. Frequency-difference beamforming results from the simulated signals integrated over the source signal's bandwidth, $11\,kHz \leq f_1 \leq 19\,kHz$, vs beam steering angle θ for ten different values of Δf, $\sum_{f_1} B(\theta, f_1, \Delta f)$. The curves proceed from $\Delta f = 195.3\,Hz$ (bottom) to $\Delta f = 1953\,Hz$ (top) in uniform steps of $195.3\,Hz$. The vertical axis is linear. Each curve is normalized by its maximum value and offset vertically by one unit from the curve below. The trade-off between angular resolution and spatial aliasing is observed as Δf increases.

each of the arrival angles of the propagation simulations, $-2.4°$, $0.3°$, and $2.6°$, which correspond to bottom-reflected, direct, and surface-reflected ray paths, respectively.

For a more complete picture, a comparison of integrated frequency-difference beamforming results is shown in Fig. 5

for a factor of 10 change in Δf for a fixed range of beam steering angle $-20° \leq \theta \leq +20°$. The ten curves proceed from $\Delta f = 195.3\,Hz$ (bottom) to $\Delta f = 1953\,Hz$ (top) in uniform steps of $195.3\,Hz$. The third curve from the top is equivalent to the one shown in Fig. 4 (solid). Here, the vertical axis of Fig. 5 is linear (not dB), and each curve is normalized by its maximum value and offset upward by one unit from the curve below. At the lowest frequency-difference (bottom), there is a single broad peak near the broadside $\theta = 0°$ without side lobes. As Δf increases, the angular resolution of the beamforming improves and the central peak separates into three peaks at the simulation ray-path angles in the middle of this figure. As Δf further increases, side lobes appear on both sides and march toward $\theta = 0°$. Interestingly, this behavior is analogous to that expected for conventional narrowband beamforming when the signal and processing frequency equals Δf. However, the frequency range of the curves shown in Fig. 5, 195.3–$1953\,Hz$, lies well below the frequency band of the broadcast signal (11–$19\,kHz$), making it more robust to potential mismatch in modeling. Thus, frequency-difference beamforming expands the possibilities for ray-path angle determination beyond those of conventional beamforming.

Sample signal waveforms that illustrate the STR blind deconvolution in the simulation are shown in Fig. 6. The top panel, Fig. 6(a), is the original signal waveform. The middle panel, Fig. 6(b), shows the simulated received signal at the shallowest array element. The bottom panel, Fig. 6(c), shows the signal waveform that is reconstructed from the simulated array measurements using STR and frequency-difference beamforming with $\Delta f = 12.21\,Hz$ [see Fig. 3(a)]. Although
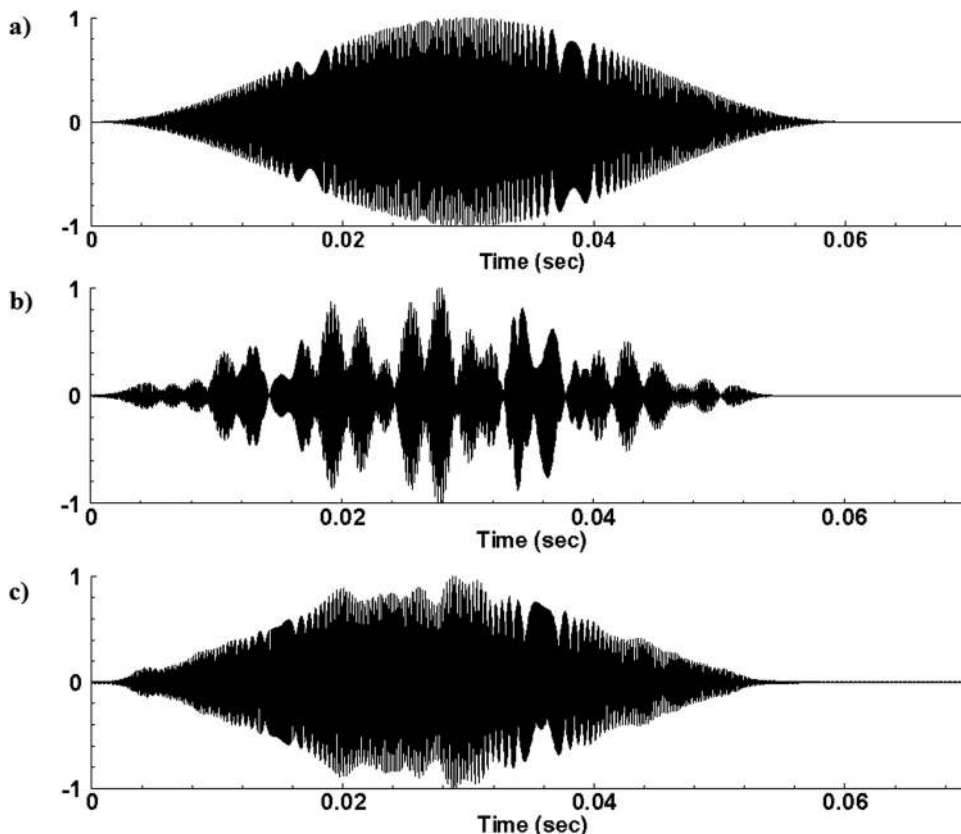

FIG. 6. Sample input and output STR signals for the simulation results: (a) broadcast signal, a cosine-tapered 60-ms, LFM sweep (11–$19\,kHz$), (b) received signal captured at the shallowest array element, and (c) STR estimated source signal using frequency-difference beamforming with $\Delta f = 12.21\,Hz$. The cross correlation coefficient of received signal with the broadcast signal is 57%. The cross correlation coefficient of the STR reconstructed signal with the broadcast signal is 98%.
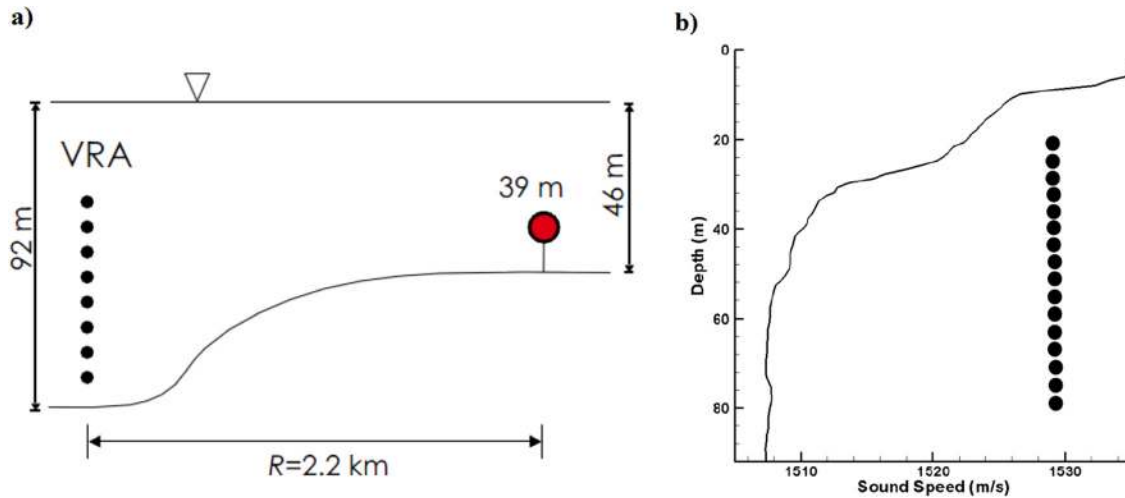
FIG. 7. (Color online) (a) FAF06 experimental geometry. The source was deployed near the bottom in 46 m of water. The receiving array, identical to that described in Fig. 1, was centered at a depth of 52.8 m in 92 m of water at a source-array range of 2.2 km. (b) A sound speed profile measured near the receiving array showing a typical downward refracting profile during the summer.

the envelope of the reconstructed signal is not perfect, the cross correlation coefficient between Fig. 6(a) and Fig. 6(c) is surprisingly good, 98%, and this result is independent of the value of $\bar{c}$. For these simulations, comparable signal reconstruction results are obtained for frequency differences as high as 48.83 Hz when $\bar{c} = 1500$ m/s.

These simulation results indicate that STR, in conjunction with frequency-difference beamforming, can provide a successful means of blind deconvolution for sparse-array recordings. Furthermore, frequency-difference beamforming allows signal-arrival angles to be determined from sparse-array recordings of broadband signals in the presence of modeling mismatch. The next section explores the extent to which these findings persist with sparse-array experimental data.

IV. STR RESULTS FROM FAF06 BROADBAND PROPAGATION MEASUREMENTS

The focused acoustic field experiment (FAF06) was conducted off the west coast of Italy in July of 2006 (Song et al., 2009; Song et al., 2010). For the receiving-array measurements used in this study, the source depth, source signal, source-array range, and vertical receiving array (VRA) geometry nominally match the simulations discussed in Sec. III. However, the actual geometry involved down slope propagation from a water depth of 46–92 m as shown in Fig. 7(a). The sound speed profile measured near the VRA is displayed in Fig. 7(b), indicating that most of the array elements are located in a nearly constant sound speed region below the thermocline. The FAF06 broadcast signals were composed of channel-probing pulses followed by communication sequences. The current blind deconvolution and beamforming results are developed from probe-pulse broadcasts with $\bar{c} = 1510$ m/s, and are provided in Figs. 8–11.

Figure 8 shows the measured signals along the array, $p_j(t)$, for a source at 42.6 m depth. Here the signal from the shallowest receiver appears as the upper-most pressure time trace and the signal from the deepest receiver appears as the lowest pressure time trace. The uneven envelopes of the signal recordings show that there was sufficient multipath propagation to distort the broadcast signal at every receiver depth. The maximum cross correlation coefficient between the FAF06 broadcast signal and any of these signals varies from 37%–75%. In addition, there is a short-duration noise pulse that follows the main transmission in the data shown in Fig. 8 in the time interval 0.05 s $< t < 0.07$ s. It has an apparent arrival angle of $25°$, and was not a part of the FAF06 signal broadcast. Such steep angle noises were observed occasionally during the experiment that were apparently due to the interaction of the long array cable with a moored surface buoy.

Figure 9 provides a comparison of beamforming results for the FAF06 signals shown in Fig. 8. Similar to Fig. 2, the
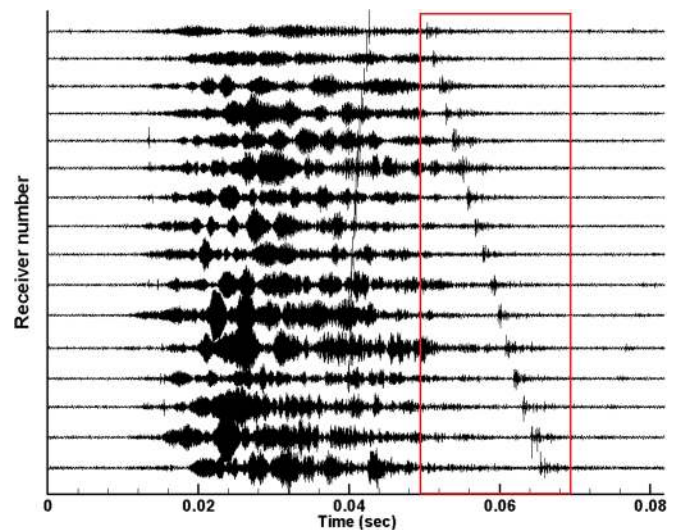

FIG. 8. (Color online) Measured FAF06 waveforms along the vertical array for a probe-signal broadcast at a source depth of 42.6 m and a source-array range of 2.2 km. The maximum cross correlation coefficient between the FAF06 broadcast signal and any of these signals varies from 37% to 75%. Note the presence of a short auxiliary noise pulse contained in the box for $t > 0.05$ s. This pulse was not a part of the FAF06 probe-signal broadcast.
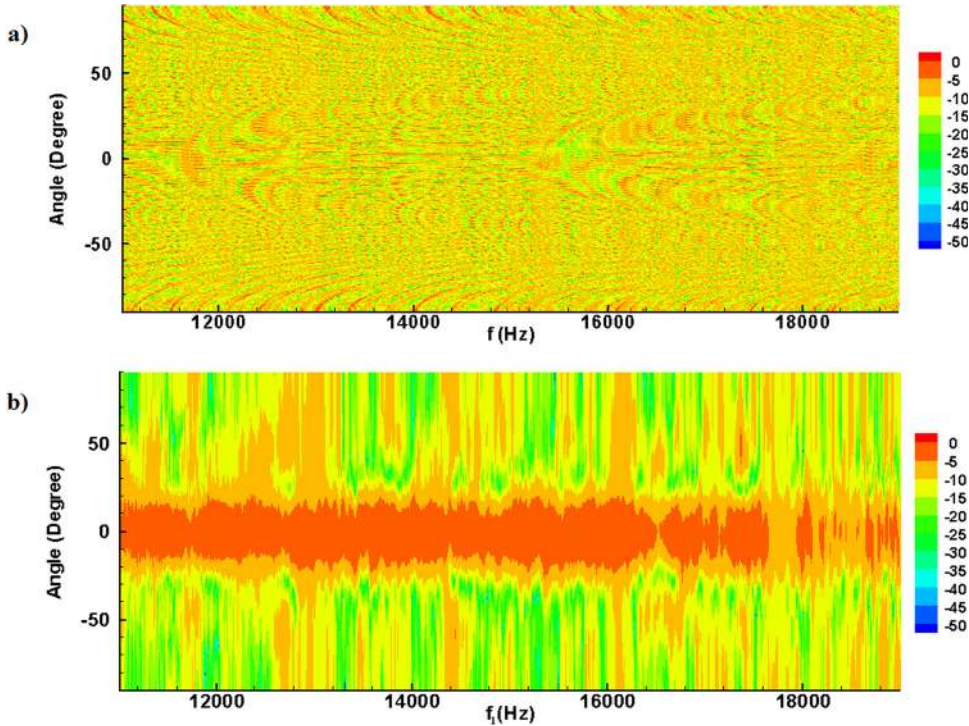
Abadi et al.: Blind deconvolution and sparse-array beamforming

FIG. 9. (Color online) Beamforming output for the measured and signals shown in Fig. 8 as a function of look angle θ and frequency f in the signal bandwidth (11–19 kHz) in dB scale: (a) conventional beamforming and (b) frequency-difference beamforming with $\Delta f = 48.83$ Hz. Similar to Fig. 2, conventional beamforming (a) is not useful while frequency-difference beamforming (b) shows signal structure centered on $\theta = 0$.

conventional beamforming result in Fig. 9(a) is featureless. In contrast, the frequency-difference beamforming result shown in Fig. 9(b) with $\Delta f = 48.83$ Hz displays a broad central ridge with an angular width of approximately 20° and resembles the corresponding simulation results in Fig. 3(b). Thus Fig. 9 confirms that the primary features of the simulation results shown in Figs. 2 and 3 persist with measured propagation data.

Figure 10 shows a comparison of source signal waveforms from the FAF06 experiment. The top waveform, Fig. 10(a), is the ideal signal of Fig. 6(a) corrected for the transmit amplitude response of the FAF06 sound projector. This is the best available estimate of the FAF06 broadcast pulse without a monitoring hydrophone that could actually measure the amplitude and phase response of the FAF06 sound projector. The lower three panels of Fig. 10 show blind
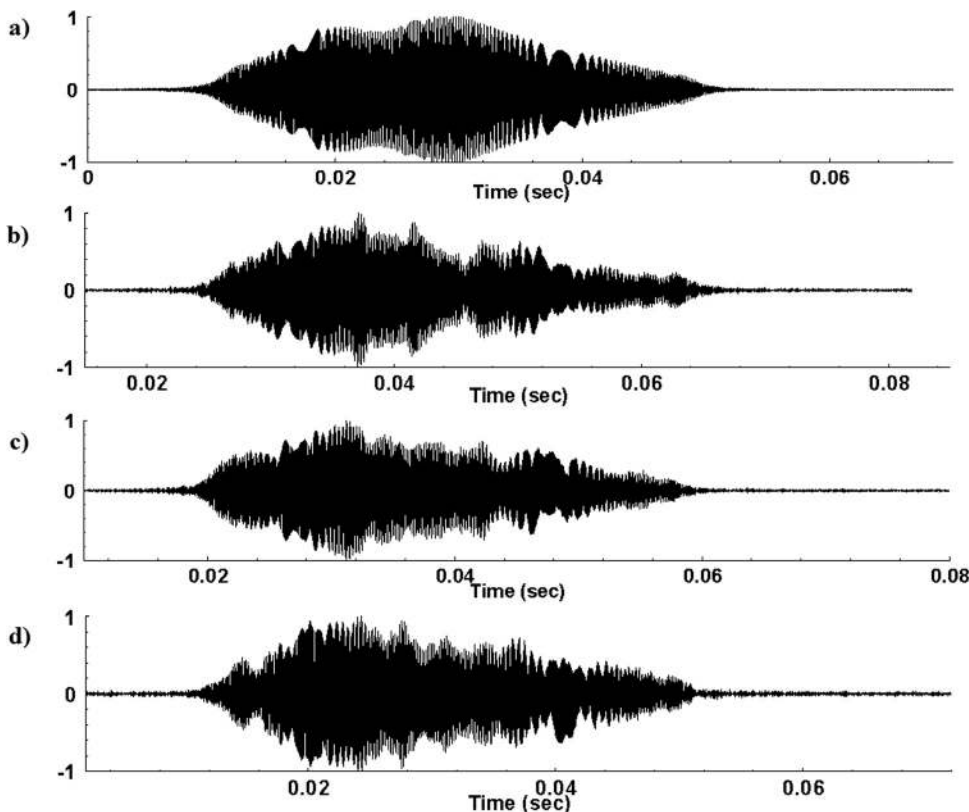

FIG. 10. Reconstructed FAF06 waveforms: (a) intended broadcast signal, a cosine-tapered 60-ms LFM sweep corrected for the projector's amplitude response, (b) STR estimated source signal using frequency-difference beamforming with $\Delta f = 12.21$ Hz at the source depth of 39 m, (c) same as (b) but recorded an hour earlier, and (d) same as (b) but for the array recordings shown in Fig. 8, which was collected 5 hours later than (b) at a source depth of 42.6 m. The cross correlation coefficients between the intended broadcast signal (a) and reconstructed signals (b), (c), and (d) are 92%, 91%, and 80%, respectively.
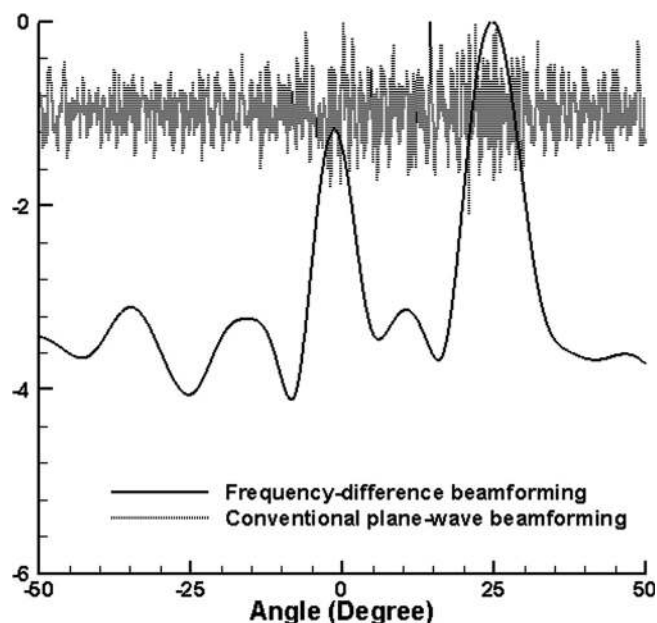
FIG. 11. Beamforming output integrated over the frequency band using the measured signals shown in Fig. 8 for $0.05\,s < t < 0.08\,s$: conventional plane-wave beamforming $\sum_f B(\theta,f)$ (dashed line) and frequency-difference beamforming with $\Delta f = 195.3\,Hz$ $\sum_{f_1} B(\theta,f_1,\Delta f)$ (solid line). The frequency-difference beamforming result displays peaks at 25° and just below 0° that correspond to the short auxiliary noise pulse and the signal's coda, respectively.

deconvolution results for the broadcast pulse using STR and frequency-difference beamforming with $\Delta f = 12.21\,Hz$. Figures 10(b) and 10(c) were recorded an hour apart with a source depth of 39 m and a source-array range of 2.2 km. The cross correlation coefficients between these two pulses and the intended broadcast pulse are 92% and 91%, respectively. This is a significant improvement over the array recordings which show an average cross correlation coefficient with the intended broadcast pulse of only 50%. Even higher cross correlations might be possible if the broadcast pulse could be more accurately compensated for the phase response of the FAF06 sound projector. The bottom waveform shown in Fig. 10 is obtained from the array recordings shown in Fig. 8. Although it came from near identical conditions that led to the pulses shown in Fig. 10(b) and 10(c), the Fig. 10(d) pulse has only an 80% correlation with the intended signal pulse. This drop in the cross correlation coefficient is caused by the presence of the short-duration noise pulse contained in the box in Fig. 8. When the Fig. 8 recordings are temporally trimmed to remove the noise pulse, the reconstructed signal's cross correlation increases to 85%. Although a cross correlation closer to 90% was expected after trimming, it was not feasible with this data because another short-duration noise pulse, at $t \approx 0.04\,s$, can be seen within main FAF06 recordings shown in Fig. 8. Thus, as currently implemented, STR loses its effectiveness when the array recordings involve multiple sources.

Figure 11 shows beamforming results integrated over the bandwidth of the signal for the portion of the FAF06 recordings shown in Fig. 8 within the box, $t > 0.05\,s$. Similar to Fig. 4, Fig. 11 shows a dashed curve for conventional beamforming and a solid curve for frequency-difference beamforming with

$\Delta f = 195.3\,Hz$. As expected, the conventional beamforming result does not indicate any ray-path arrival angles. However, the frequency-difference beamforming result correctly indicates the arrival angle of the signal-coda, just below 0°, and the arrival angle of the short auxiliary noise pulse, 25°. Although signal arrival angles for the FAF06 probe-pulse broadcasts can be estimated with frequency-difference beamforming, they are not reported here because the downward refracting sound speed profile shown in Fig. 7 causes all ray paths to interact with sea floor and there is insufficient knowledge of the FAF06 environment (e.g., bathymetry and geoacoustic properties) to perform accurate ray-trace calculations for comparison. Nevertheless, Fig. 11 indicates that frequency-difference beamforming potentially has general applicability for identifying signal-arrival directions for acoustic data gathered with sparse receiving arrays since the 25° arrival angle for the short noise pulse can be determined graphically from Fig. 8 with the known array geometry and $\bar{c} \approx 1510\,m/s$.

V. SUMMARY AND CONCLUSIONS

Synthetic time reversal (STR) is a computationally simple means for blind deconvolution of array-recorded sounds that have propagated from an unknown source to a receiving array through an unknown multipath environment. This study has explored the performance of STR with simulated and measured underwater propagation data when the receiving array was extremely sparse and conventional beamforming of the array recordings was not useful.

The following conclusions can be drawn from this research effort. (1) STR blind deconvolution was successful, with simulation and experimental data, even when the receiving array was too sparse for conventional beamforming. When the array-recorded sounds come from a single source, the cross correlation coefficient between the broadcast signal and the STR reconstructed signal are routinely above 90%. (2) These STR results are robust because a single propagating mode or ray path does not need to be isolated by the receiving array. In fact, the highest cross correlations between the source-broadcast and STR-estimated signals in this study were commonly obtained from frequency-difference beamforming when the angular resolution of the receiving array was the lowest possible, that is, when the frequency difference was the lowest possible. (3) However, as currently implemented, the performance of STR was degraded when sounds from multiple sources arrive simultaneously at the receiving array. (4) To achieve these sparse-array blind deconvolution results with STR, unconventional frequency-difference beamforming was developed to estimate the phase signature of the unknown source signal. Except for possible mathematical similarities with the quadratic non-linearity exploited for the parametric acoustic array (Westervelt, 1963), frequency-difference beamforming appears to be novel to the best of our knowledge, and it may be useful in applications of array signal processing beyond blind deconvolution. In (5) frequency-difference beamforming can be used with a sparse receiving array in the presence of modeling mismatch to isolate signal-path arrival angles when conventional beamforming fails to do so.

Abadi *et al.*: Blind deconvolution and sparse-array beamforming

ACKNOWLEDGMENTS

Abadi, S. H., Rouseff, D., and Dowling, D. R. (**2012**). "Blind deconvolution for robust signal estimation and approximate source localization," J. Acoust. Soc. Am. **131**, 2599–2610.

Broadhead, M. K., and Pflug, L. A. (**2000a**). "Performance of some sparseness criterion blind deconvolution methods in the presence of noise," J. Acoust. Soc. Am. **107**, 885–893.

Broadhead, M. K., and Pflug, L. A. (**2000b**). "Use of higher order statisitics in source signature estimation," J. Acoust. Soc. Am. **107**, 2576–2585.

Dzieciuch, M. A., Worcester, P. F. W., and Munk, W. H. (**2001**). "Turning point filters: Analysis of sound propagation on a gyre-scale," J. Acoust. Soc. Am. **110**, 135–149.

Kinsler, L. E., Frey, A. R., Coppens, A. B., and Sanders, J. V. (**2000**) *Fundamentals of Acoustics*, 4th ed. (Wiley, New York), pp. 191–192.

Martins, N., Jesus, S., Gervaise, C., and Quinquis, A. (**2002**). "A time-frequency approach to blind deconvolution in multipath underwater channels," in *Proceedings of ICASSP'02* (IEEE, New York), pp. 1225–1228.

Roan, M. J., Gramann, M. R., Erling, J. G., and Sibul, L. H. (**2003**). "Blind deconvolution applied to acoustical systems identification with supporting experimental results," J. Acoust. Soc. Am. **114**, 1988–1996.

Rouseff, D., Jackson, D. R., Fox, W. L. J., Jones, C. D., Ritcey, J. A., and Dowling, D. R. (**2001**). "Underwater acoustic communication by passive phase conjugation: Theory and experimental results," IEEE J. Ocean. Eng. **26**, 821–831.

Roux, P., Cornuelle, B. D., Kuperman, W. A., and Hodgkiss, W. S. (**2008**). "The structure of raylike arrivals in a shallow-water waveguide," J. Acoust. Soc. Am. **124**, 3430–3439.

Sabra, K. G., and Dowling, D. R. (**2004**). "Blind deconvolution in oceanic waveguides using artificial time reversal," J. Acoust. Soc. Am. **116**, 262–271.

Sabra, K. G., Song, H. C., and Dowling, D. R. (**2010**). "Ray-based blind deconvolution in ocean sound channels," J. Acoust. Soc. Am. **127**, EL42–EL47.

Sibul, L. H., Roan, M. J., and Erling, J. (**2002**). "Deconvolution and signal extraction in geophysics and acoustics," J. Acoust. Soc. Am. **112**, 2389.

Siderius, M., Jackson, D. R., Rouseff, D., and Porter, R. (**1997**). "Multipath compensation in shallow water environments using a virtual receiver," J. Acoust. Soc. Am. **102**, 3439–3449.

Siderius, M., Porter, M. B., Hursky, P., McDonald, V., and the KauaiEx Group. (**2007**). "Effects of ocean thermocline variability on noncoherent underwater acoustic communications," J. Acoust. Soc. Am. **121**, 1895–1908.

Smith, G. B. (**2003**). "Multipath compression by multiple convolutions," J. Acoust. Soc. Am. **113**, 2213.

Smith, J. F., and Finette, S. (**1993**). "Simulated annealing as a method of deconvolution for acoustic transients measured on a vertical array," J. Acoust. Soc. Am. **94**, 2315–2325.

Song, H. C., Hodgkiss, W. S., Kuperman, W. A., Akal, T., and Stevenson, M. (**2009**). "High frequency acoustic communications achieving high bandwidth efficiency (L)," J. Acoust. Soc. Am. **126**, 561–563.

Song, H. C., Hodgkiss, W. S., Kuperman, W. A., and Stevenson, M. (**2010**). "High-rate multiuser communications in shallow water," J. Acoust. Soc. Am. **128**, 2920–2925.

Taxt, T., and Strand, J. (**2001**). "Two-dimensional noise-robust blind deconvolution of ultrasound images," IEEE Trans. Ultrason. Ferroelectr. Freq. Control **48**(4), 861–866.

Weber, R., and Bohme, J. F. (**2002**). "Adaptive super-exponential methods for blind multichannel equalization," in *Sensor Array and Multichannel Signal Processing Workshop* (IEEE, New York), pp. 585–589.

Westervelt, P.J. (**1963**). "Parametric acoustic array," J. Acoust. Soc. Am. **35**, 535–537.

Xinhua, Z., Anqing, Z., Jianping, F., and Shaoquing, Y. (**2001**). "Study on blind separation of underwater acoustic signals," in *Proceedings ICSP2000* (IEEE, New York), pp. 1802–1805.

Yu, C., Zhang, C., and Xie, L. (**2012**). "A blind deconvolution approach to ultrasound imaging," IEEE Trans. Ultrason. Ferroelectr. Freq. Control **59**(2), 271–280.

Zeng, W.-J., Jiang, X., Li, X.-L., Zhang, X.-D. (**2009**). "Deconvolution of sparse underwater acoustic multipath channel with a large time-delay spread," J. Acoust. Soc. Am. **127**, 909–919.

Ziomek, L. J. (**1993**). "Three necessary conditions for the validity of the Fresnel phase approximation for the near-field beam pattern of an aperture," IEEE J. Ocean. Eng. **18**(1), 73–75.